Solar Energy 262 (2023) 111821

Contents lists available at ScienceDirect

Solar Energy

journal homepage: www.elsevier.com/locate/solener

High resolution imaging spectroscopy of the sky

Yiwei Mao [a,b,*], Chris H. Lee [c], Charles M. Bachmann [b,c], Bradley J. Evans [b,d], Iver H. Cairns [a,b]

[a] School of Physics, The University of Sydney, Sydney, 2006, NSW, Australia
[b] ARC Training Centre for CubeSats UAVs & their Applications, The University of Sydney, Sydney, 2006, NSW, Australia
[c] Chester F. Carlson Center for Imaging Science, Rochester Institute of Technology, Rochester, 14623, NY, United States of America
[d] School of Environment and Rural Science, University of New England, Armidale, 2351, NSW, Australia

ARTICLE INFO

Keywords:
Radiance
Luminance
Solar spectrum
Diffuse scatter
Imaging spectroscopy
Hyperspectral

ABSTRACT

Diffuse sky radiance is a key variable for resolving the global energy budget, weather forecasting, radiative transfer modelling and estimating solar energy potential at the Earth's surface. This study is the first attempt to directly measure a full-sky view of the sky radiance using a pushbroom imaging spectrometer. We mounted the open-source hyperspectral imager (OpenHSI) on a tripod and rotation stage during a clear day in Rochester, NY, USA, and resampled the swaths to a sphere using the HEALPix projection. We achieved a 0.45° angular resolution, which is an order of magnitude better than any previous experimental study. Our results showed agreement with analytic studies using radiative transfer codes, and with photometric studies, demonstrating a strong wavelength dependence for sky radiance distributions. Along the principal plane, we observed a spectral steepening that transitioned from predominantly Mie scattering in the circumsolar region to predominantly Rayleigh scattering. We also compared our results to a CIE standard clear sky. Although all the data were collected within one hour, the movement of the Sun during this time is noticeable in the results. Nevertheless, our study provides confidence in using existing models and introduces a new technique for high resolution mapping of the sky radiance distribution using pushbroom imaging spectrometers.

1. Introduction

During the day, the surface of the Earth is illuminated directly by light from the Sun, and a significant fraction of this energy is scattered by small liquid or solid particles suspended in the atmosphere. This fraction varies based on fluxes in atmospheric chemical composition. The diffuse radiation from the sky is dominated by the process of Rayleigh scattering on a clear day as blue light is strongly scattered, with some Mie scattering caused by aerosols in the atmosphere. On cloudy or overcast days, the sky appears grey due to the increased diffusion of light, driven by the presence of the water vapour in the clouds.

For remote sensing studies, estimating the reflective properties of the Earth's surface requires accurate prediction of solar radiance and atmospheric conditions. Process-based models estimate the physical processes in the atmosphere, such as radiative transfer models. For instance, [1] simulated the sky radiance for various aerosol profiles at a resolution of 1° in elevation and 2° in azimuth, and varied the sun zenith angle.

Early theoretical studies in atmospheric scattering focused on modelling the gradation and scattering indicatrix [2,3] for the purposes of predicting indoor natural lighting conditions for various sky conditions. More studies were motivated by a desire for energy conservation by improving indoor lighting conditions. These studies produced sky luminance distributions in various cities around the world [4–7]. The applications included indoor illuminance [8,9], sky-view factors and urban heat [10–12], and analysis of shading [13–16].

Radiation-aerosol-cloud interactions in the atmosphere, specifically the processes of absorption and scattering, have a significant effect on the Earth's energy budget, and subsequently our ability to accurately model the processes. [17] reported significant uncertainties: 30% uncertainty in estimating aerosol direct forcing, and 100% uncertainty in estimating aerosol-cloud interactions. Recommendations from [17] included investigations into better understanding radiation-aerosol interactions in the atmosphere and specifically radiation-cloud-aerosol interactions. Key to achieving this understanding is better characterising the sky viewed from both space and Earth.

In other applications, the power production of photovoltaic cells, which are spectrally sensitive, was evaluated in a variety of sky conditions and partial shade [18–20], in particular, to optimise the incidence angle [19,21]. Furthermore, spectral sky radiance was studied in

* Corresponding author at: School of Physics, The University of Sydney, Sydney, 2006, NSW, Australia.
E-mail address: yiwei.mao@sydney.edu.au (Y. Mao).
URL: https://openhsi.github.io/openhsi/ (Y. Mao).

https://doi.org/10.1016/j.solener.2023.111821
Received 23 April 2023; Accepted 23 June 2023
Available online 12 July 2023

forestry to predict the distribution of light under canopies [22–25], and in biology to calculate vitamin D absorption in humans [26]. Rendering realistic sky scenes in computer games also requires accurate models of the sky radiance distribution [27–30].

Estimates of sky luminance were obtained using a CCD camera and fisheye lens, providing high temporal resolution but yielded 5%–20% deviations from a separate spectroradiometer [31]. This was then followed by [32] who employed additional camera setups and a sunshade to evaluate the relation between windows and indoor luminance. They separated the dome into 145 sky patches according to CIE 1994 [33], with an angular resolution of around 11°. Scientists also used almucantars with a narrow field of view lens [7] to map sky luminance.

In this work, we focused on measuring the diffuse sky scatter in the visible to near-infrared range on a clear day. The goal was to map the sky near solar noon at a <1° resolution and include ground targets for analysis. We wanted to evaluate the wavelength dependence of sky radiance in the presence of an atmosphere exhibiting Rayleigh scattering from gas molecules and Mie scattering from aerosols with an angular resolution better than previous experimental studies. As far as we know, this is the first study to map the sky at such a fine resolution using a pushbroom imaging spectrometer.

The following section will describe the methodology to combine multiple hyperspectral swaths to a data-sphere. This is followed by discussion of the distribution of diffuse radiation as it varies by wavelength and zenith angle. Finally, limitations of this study and key findings are summarised.

Fig. 1. The OpenHSI hyperspectral imager scans the sky from a tripod and rotation stage. We set up the camera and Spectralon™ panel on the roof to minimise occlusions.

2. Method

We used the open-source hyperspectral imager OpenHSI [34] to sweep across the sky, recording spectral radiance in the visible near-infrared from 430–900 nm. The compact and lightweight nature of the pushbroom instrument allowed the camera to be mounted on a tripod and rotation stage, as depicted in Fig. 1. On the roof of the Chester F. Carlson Center for Imaging Science at the Rochester Institute of Technology (43.0848° N, 77.6715° W), we performed this experiment under clear sky conditions on October 24th 2022, soon after solar noon.

The tripod's azimuth position was controlled with one knob against a protractor and the elevation angle was controlled by a rotation stage, which swept out 360° along great circles at 15°/s. Due to the narrow field-of-view of 11°, multiple swaths were necessary to cover the full sky. We acquired 34 imagery swaths targeting 50% overlap, including the start and end positions. Being near the roof edge allowed the camera to see more of the car park and straight roads, which was a key feature to ensure the azimuthal positions could be verified and fine-tuned between swaths. An accurate parametric model also allowed the start and end swaths to be aligned.

A Spectralon™ panel was placed in the field of view to facilitate an empirical reflectance calculation. To maximise signal, an exposure time of 15 ms was chosen, as this was the limit just before the digital counts saturated when the camera was pointed at the Spectralon™ panel. Over the course of an hour of data collection, the solar zenith angle shifted from 58° to 65°. An inclinometer was used to verify the camera orientation. Despite changing the exposure time, direct sunlight always saturated the sensor, so the circumsolar region needed to be masked once the data were mosaiced and resampled.

Fig. 2 depicts the steps to turn raw pushbroom hyperspectral data into a spectral radiance data-sphere.

2.1. Removing dead-time and spectral radiance

Since the control of the rotation stage and camera were independent of each other, we let the camera start recording *before* the rotation and only ended recording after a full rotation was completed. While dead-time is apparent in the unchanging spatial–spectral portion at the beginning and end of each swath, the time delay between the start of recording and rotation was not consistent. To automate the clipping of dead-time, a Sobel filter in the along-track direction was used on a greyscale image and a peak finding algorithm returned the appropriate along-track pixels to remove.

The raw data were corrected for smile error, converted to radiance, and binned to 3 nm bands using the OpenHSI software package [34].

2.2. Reconciling azimuth and elevation between adjacent swaths

Despite having a 360° protractor fixed to the tripod to assist in ensuring a separation of 6° between swaths, any small error would result in misalignment between the start and end of the image swaths. Since standard pattern matching with similar features relies on having no curvature, the same technique cannot be applied to the image swaths collected. While possible for local features, each swath fundamentally has curvature. Additionally, the rotation of the camera reverses the perspective of left and right after reaching zenith. Therefore, visual inspection of similar features was required. Examples of the RGB composites used are shown in Fig. 3, where the shift in azimuth can be adjusted.

Due to the physical constraint of mounting a rotation stage, the camera was displaced from the tripod centre, causing parallax for any closeby objects in Fig. 3. This can be seen in the misalignment of the nearby roof railing and shadows. In the far field, this is not an issue, since there are fewer pixels due to the smaller angular displacement covered. We found that roads and cars assisted best in aligning straight edges and colours. The same features were used to adjust any elevation shifts.

2.3. Assigning azimuth and elevation angles

Each swath corresponded to a section from a sphere as shown in Fig. 4(a). The pixels in each swath were assigned an azimuth and elevation angle, although not every pixel was necessary to cover the whole sphere. From spherical geometry, the area for a slice of constant azimuth is bound by two sinusoids. See Fig. 4(b) for a visual representation.

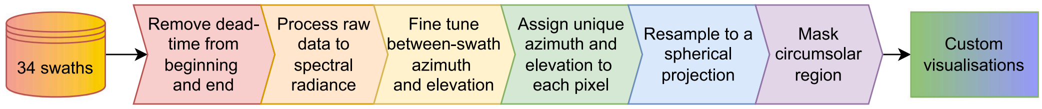

Fig. 2. Flowchart of steps to take raw data to final form.

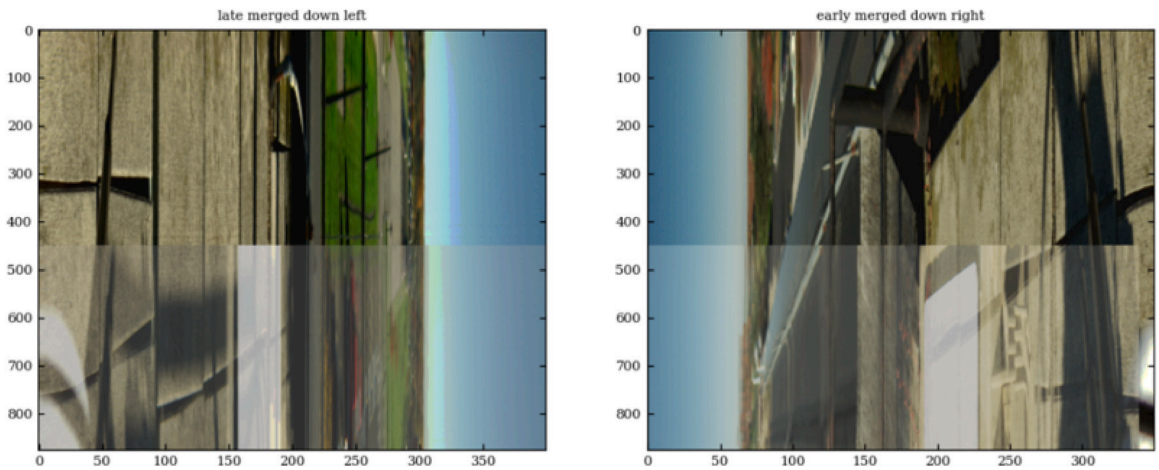

Fig. 3. Overlaying a translucent swath shifted over another swath. The shift can be adjusted until objects in the far field align. The nearby railings suffered from parallax so we used straight lines from far-field roads and car colours to fine-tune the azimuth shift.

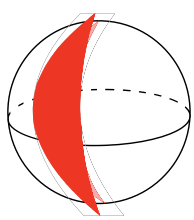

(a) Overlay of a swath section onto a sphere. The mask is defined by the shaded region.

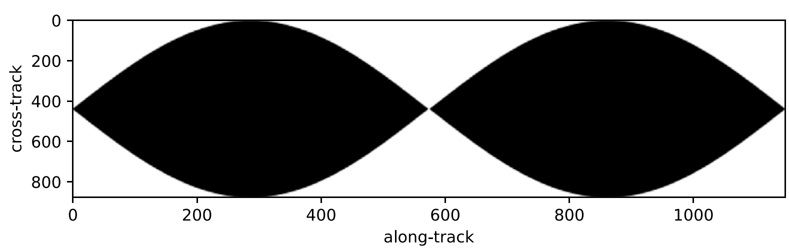

(b) For each swath, only the black region bounded by sinusoidals is required. The nodes represent the poles in spherical coordinates.

Fig. 4. Mask applied to each swath. The shaded region corresponds to an 11° change in azimuth set by the field of view of the OpenHSI camera.

2.4. Resampling to a spherical projection

Once each pixel has a unique azimuth and elevation, we need to resample the data onto a spherical grid. We used the Hierarchical Equal Area isoLatitude Pixelization (HEALPix) projection, which is commonly used in astronomy to create maps of the cosmic microwave background [35]. This projection has the useful property that each pixel covers the same surface area. We set the HEALPix parameter `nside` to 128, balancing the tradeoff between data size and resolution, and resulting in an angular resolution of 0.45°. Since the `healpy` Python library [36] only supports scalar heatmaps, we developed routines to enable it to work with spectral data-spheres. When multiple swath pixels corresponded to the same sky pixel, we took the average.

2.5. Masking invalid pixels

The final step was to mask pixels where the sensor saturated near the Sun. Therefore, we masked any pixel with any wavelength component that saturated the sensor. These pixels were subsequently masked in visualisations.

3. Results and discussion

An RGB composite image of the processed data-sphere is shown in Fig. 5. Even though we were on the roof, other buildings at the Rochester Institute of Technology obstructed part of the horizon. Other than the bright circumsolar region, the horizon also appeared brighter than the rest of the sky due to the longer atmospheric pathway for light to scatter before reaching the sensor. Since the Spectralon™ panel at approximately −40° elevation shifted positions between swaths, the resampling scheme caused some "seams" to appear.

For reference, a panorama taken with a phone during data collection is shown in Fig. 6. Located near the roof edge, the OpenHSI camera had vantage of the roads and carpark below, which proved important for fine-tuning the azimuth angle between adjacent swaths.

In Fig. 7, the sky dome is shown for 450, 550, 650, and 750 nm. The radiance appeared most isotropically distributed in the blue (band 450 nm), and the distribution became more anistropic as wavelength increased. This is consistent with what we expect for Rayleigh scattering. At 750 nm, almost the entirety of the power was concentrated around the circumsolar region. The highest intensity was observed in the circumsolar region between 500 and 550 nm, which is not surprising given that this range is close to the wavelengths with peak solar power expected for the Sun's blackbody spectrum.

Fig. 8 shows the spectral radiance for the same wavelengths as Fig. 7, but now using a Mollweide projection to include ground features. The increase in radiance at 750 nm for the well-maintained university lawns (see the bright feature below the horizon at 300–180°

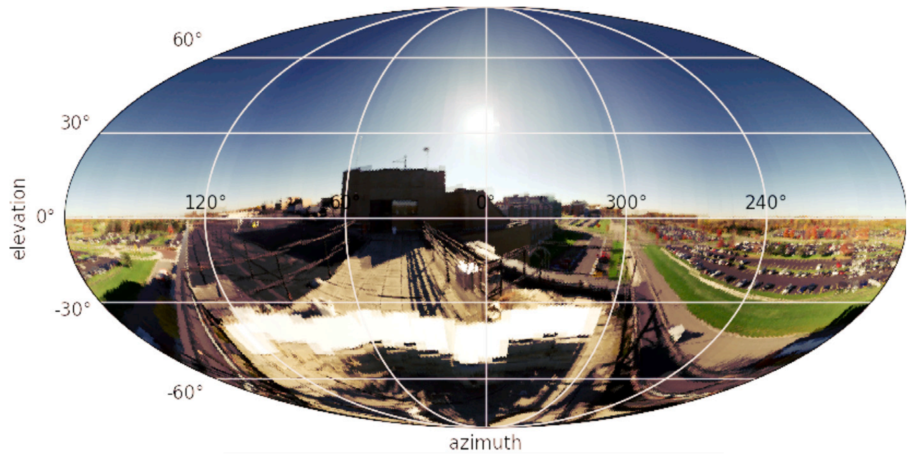

Fig. 5. Mollweide projection of the data-sphere with selected red (640 nm), green (550 nm), and blue (470 nm) bands. Histogram equalisation was applied. The solar zenith angle was 58° and the patch of white around −40° elevation was the Spectralon™ panel which was moved between subsequent swath collections.

Fig. 6. Rooftop panorama overlooking a carpark and forests taken with a phone camera. Near the camera and tripod is a Spectralon™ panel and railings.

azimuth), compared to at 650 nm, is a sign of chlorophyll rich vegetation. From the changing positions of the Spectralon™ panel, we can also observe the angular dependence of the bidirectional reflectance distribution function. While raised on a box to minimise dust blowing onto the surface, the uneven floor caused a small tilt so the panel appeared brightest at an azimuth of 330° rather than the expected 0°.

3.1. Luminance

By integrating the spectral radiance L with a photopic luminosity function $y(\lambda)$ across wavelengths λ, we obtain the luminance

$$L_v = K \int_0^\infty y(\lambda) L(\lambda) d\lambda \quad (1)$$

where K is 683 lm/W. The photopic luminous efficiency function y, shown in Fig. 9, is based on the response of the human eye and is thus appropriate for assessing daylighting.

The experimentally measured luminance of our sky dome is shown in Fig. 10(a) normalised to zenith. It contains features that indicate a clear day: the anisotropic bright circumsolar region, a bright ring around the horizon, and a darker region approximately 90° away from the Sun. This also appears consistent with the characterisation of the five CIE standard clear skies presented in [37] where the subtle changes in the dark section depend on atmospheric aerosols and turbidity.

The simulated luminance [38] was based on the historical EnergyPlus weather data [39] from the Rochester International Airport situated 4 km from Rochester Institute of Technology. The estimated CIE sky parameters were used in the Perez model and the result is seen in Fig. 10(b).

We expected the circumsolar brightening to be symmetric but Figs. 7, 8, and 10(a) show the circumsolar side opposite the building to appear slightly fainter. This is due to a 15 min delay in data collection as we backed up data and the associated changes in the Sun's position. Despite using the minimum exposure time, direct exposure to the Sun saturated our sensor so we masked affected pixels. Nonetheless, the

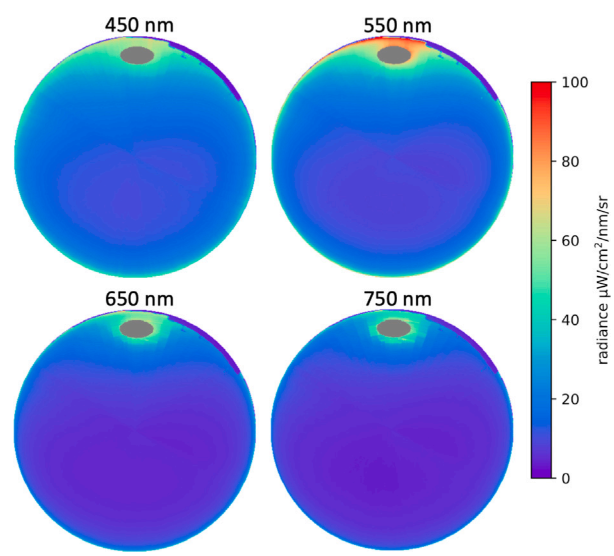

Fig. 7. Orthographic projections of the spectral radiance for various wavelengths. The solar zenith angle was 58°. Saturated pixels were masked. The minor asymmetry in isotropic scatter is due to a 15 min time delay during data collection.

circumsolar behaviour is a defining characteristic of a clear day. The closest CIE sky type was Standard Clear Sky 14: cloudless turbid sky with broad corona.

The horizon brightening effect in our measured luminance appeared more intense than the simulated Perez equivalent (compare Figs. 10(a) and 10(b) below 10° elevation). Our measurements appear to be consistent with simulated radiative transfer studies such as [1]. Our results indicate that the Perez sky model underestimates the horizon

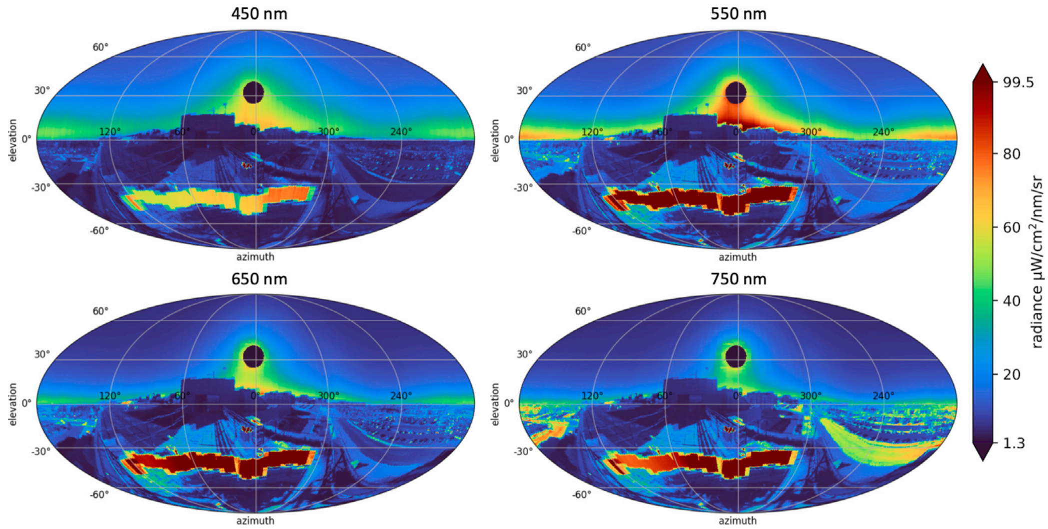

Fig. 8. Mollweide projections of the spectral radiance data-sphere for various wavelengths. The solar zenith angle was 58°. Saturated pixels were masked and the colour scale was capped between the 2%–98% percentiles.

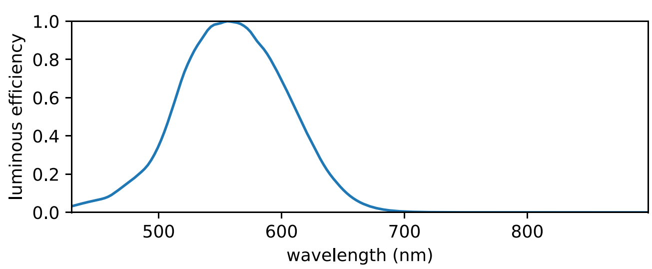

Fig. 9. The photopic luminous efficiency function, interpolated to the OpenHSI wavelengths.

brightening due to multiple scattering effects near the ground surface, which is unaccounted for and is site specific.

3.2. Principal plane

In radiative transfer, Rayleigh scattering in the sky is modulated by two functions [40] called the indicatrix and gradation. The principal plane is the vertical plane containing the solar incidence angle and the view zenith angle. Along this plane corresponding to the indicatrix, we observed a peak in the radiance in the circumsolar region. For a clear sky, the indicatrix is approximately proportional to $1 + \cos^2\theta$ where θ is the angle between the solar zenith angle and a position along the principal plane. Near $\theta = 90°$ corresponding to a sky pixel zenith angle of $-32°$, we observed the theoretical minimum. This phenomenon is seen in Fig. 11 where the spectral radiance for selected visible bands decreases further away from the Sun before gradually rising again near the horizon ($\theta = -90°$). As demonstrated by the separation between the curves at the minimum point, blue light was scattered more strongly than red light.

Fig. 12 shows the spectral radiance along the principal plane as the solar zenith angle increases from 5° towards the horizon. Close to the Sun within the circumsolar region, the diffuse radiance is dominated by Mie scattering from aerosols and particulates in the atmosphere. The effect of this is an almost white glare and this is seen by the spectrally flat curve at 5°. As the zenith angle approaches 90°, the curves gradually become steeper. This corresponds to a transition from predominantly Mie scattering to predominantly Rayleigh scattering. From the dotted lines which indicate the wavelength raised to select integer exponents, the radiance at $\theta = -90°$ appears to sit between λ^{-3} and λ^{-4}. Pure Rayleigh scattering would have a λ^{-4} relation so this is an indication of minor contributions from Mie scattering. Beyond this point, as the angle approaches the horizon, the radiance increases again but retains its slope.

Dividing by the Sun's blackbody spectral radiance, we can quantify the scattering component without also seeing the effects of a blackbody emission spectrum. In Fig. 12, we still observe the steepening of the radiance curves towards the minimum point and the effects of horizon brightening. The slope is approximately λ^{-3} indicating a mixture of Rayleigh and Mie scattering.

3.3. Limitations and future work

Despite our best efforts to mosaic neighbouring swaths accurately, the stitching and resampling process created noticeable seams. Part of this is due to the change in the solar zenith angle, increasing from 58° to 65° during data collection. A more accurate rendering of the continuous distribution of diffuse scattering could be achieved by weighting the boundary pixels of each swath less in the resampling process. While we expected a symmetry about the principal plane, this was offset marginally and some sections of the sky appeared fainter; this corresponded to the 15 min time delay while backing up data midway through collection. Future field experiments would need to consider the tradeoff between angular resolution and time required for data collection. While the lightweight and compact form factor of the OpenHSI camera made this experiment possible, the narrow field view of 11° increased the number of swaths needed to completely scan the sky.

The main challenges to using this setup were a sturdy tripod and a smooth actuating rotation stage. Our first attempt with a small rotation stage exhibited knocking when the mounted camera caused an off-axis load. We settled on the Standa SM 13846 which could handle the weight, and the high torque meant full rotation could be achieved at more or less constant speed, with negligible acceleration time. A second rotation stage in azimuth could be used to fully quantify a parametric model and forego the manual fine-tuning of azimuth angles. This is something to consider when mounting other imaging spectrometers to scan the sky.

Our results presented here are specific to the atmospheric conditions in Rochester, NY, USA during a cloudless sky. Future work could use the Spectralon™ panel we placed within each swath to evaluate the relationship between sky and ground. Finally, more data collected over a wide variety of solar zenith angles and polarimetric studies could be used to build and fine-tune the predictive power of analytic models.

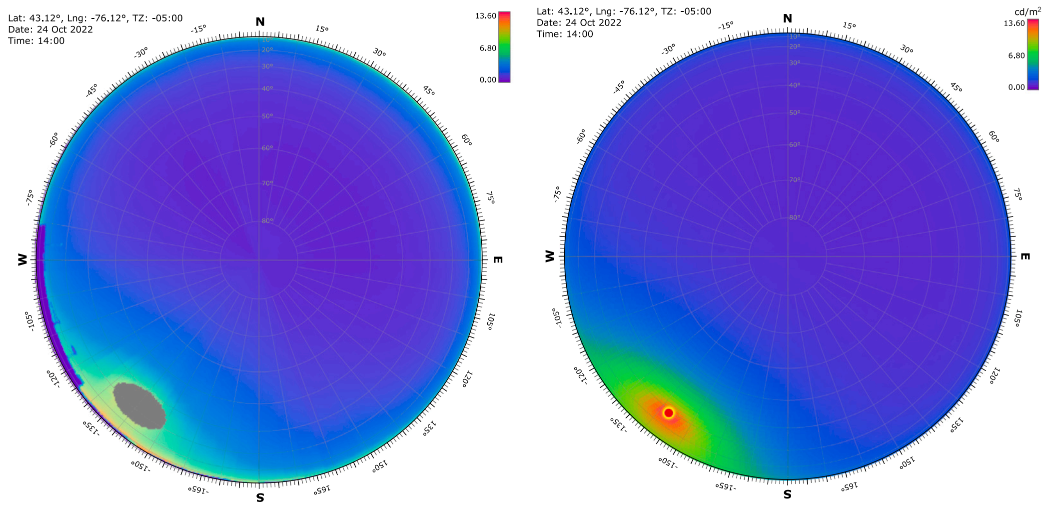

(a) Measured luminance normalised to zenith. The building near the Sun occludes some of the horizon. Saturated pixels are masked.

(b) Simulated luminance using the Perez sky model and historical data for the specified day and time. This corresponds to CIE Standard Clear Sky 14: cloudless turbid sky, broad corona

Fig. 10. Experimentally measured and simulated luminances for a clear day in Rochester, NY, USA. We used the orthographic projection for this visualisation. We measured more horizon brightening compared to the Perez sky model.

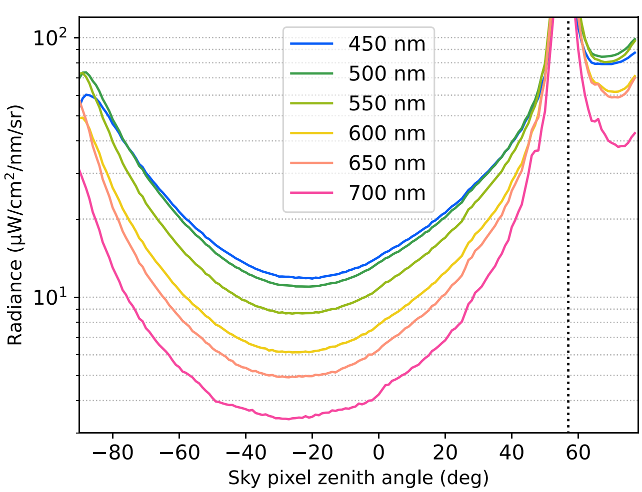

Fig. 11. The spectral radiance in the principal plane. The vertical dotted line indicates the solar zenith angle. The region in the circumsolar region is not shown due to sensor saturation. Minimum appears close to 90° away from solar zenith.

4. Conclusions

High resolution imaging spectroscopy of the entire sky allows for more accurate estimation of atmospheric parameters and prediction of available solar energy for remote sensing applications, indoor daylighting design, aerosol modelling, and power production for photovoltaics. This work describes the first attempt to use a pushbroom imaging spectrometer to directly measure diffuse sky radiance of the whole sky and surroundings using a tripod and a rotation stage. The compact and lightweight nature of the open-source hyperspectral imager (OpenHSI) made this setup possible. We solved the challenge of mosaicing swaths on a sphere and resampling spectral data with the HEALPix projection. The end result is a radiance data-sphere at 0.45° angular resolution (a magnitude better than previous experimental studies) containing both the sky and ground features. We showed that diffuse scattering on a clear day is mostly isotropic for short wavelengths and strongly anisotropic for longer wavelengths past blue. We compared our measured luminance to a simulated Perez model, revealing a more intense horizon brightening in our results which we hypothesise to be due to multiple scattering near the ground. In the principal plane, the minimum appeared approximately 90° from the solar zenith as predicted by the indicatrix function. At this minimum point, we showed that the spectral fall-off is close to λ^{-3} after normalising by the Sun's blackbody spectrum, indicating Rayleigh scattering and small contributions from Mie scattering. These results agree with analytical studies done with radiative transfer codes, and with experimental studies of sky luminance.

While our experiment is specific to the atmospheric conditions in Rochester, NY, USA, and time of day, it provides confidence in the use of analytic models and a new methodology for future experiments with other imaging spectrometers. By streamlining the data collection, the movement of the Sun's position in the sky can be minimised. Our results will inform stakeholders in efficient daylighting, the prediction of photovoltaic energy output in partial shading, and the modelling of atmospheric aerosols.

Funding

This research was conducted by the ARC Training Centre for Cubesats, UAVs and their Applications (CUAVA - project number IC170100023) and funded by the Australian Government.

Declaration of competing interest

The authors declare that they have no known competing financial interests or personal relationships that could have appeared to influence the work reported in this paper.

Acknowledgements

The authors acknowledge Prof. Jan van Aardt in proofreading the manuscript.

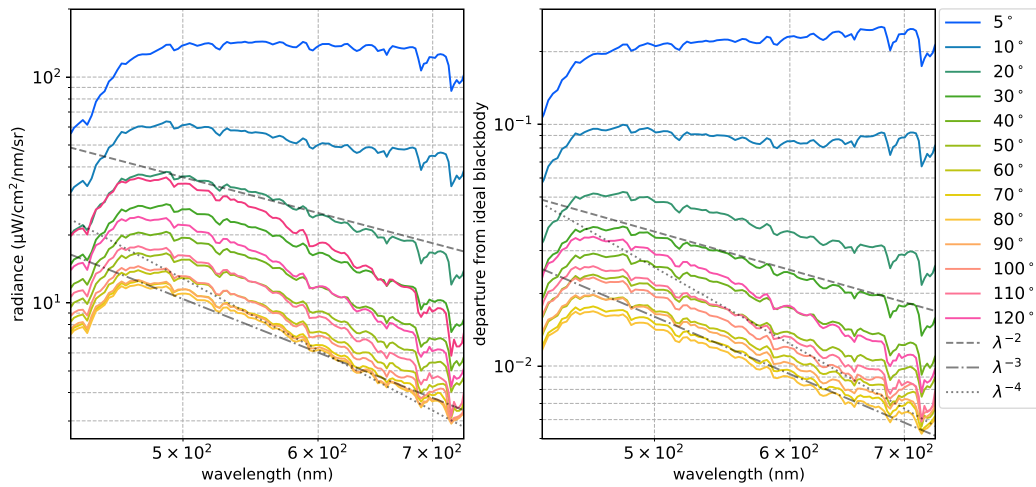

Fig. 12. Left: Radiance of sky pixels along the principal plane. Near the Sun, the combination of Rayleigh and Mie scattering causes a white glare. Away from the Sun, the spectral fall-off approaches λ^{-4}. Right: Departure from an ideal blackbody. The spectral radiance curves still show a decreased slope away from the Sun and then the radiance increases again near the horizon. Dashed lines for λ^{-2}, λ^{-3}, and λ^{-4} were added for reference.

References

[1] C.A. Gueymard, M. Kocifaj, Clear-sky spectral radiance modeling under variable aerosol conditions, Renew. Sustain. Energy Rev. 168 (2022) 112901.

[2] R. Kittler, Some qualities of scattering functions defining sky radiance distributions, Sol. Energy 53 (6) (1994) 511–516.

[3] A.P. Brunger, F.C. Hooper, Anisotropic sky radiance model based on narrow field of view measurements of shortwave radiance, Sol. Energy 51 (1) (1993) 53–64.

[4] D.H. Li, C.C. Lau, J.C. Lam, Evaluation of overcast-sky luminance models against measured Hong Kong data, Appl. Energy 70 (4) (2001) 321–331.

[5] S. Chirarattananon, P. Chaiwiwatworakul, Distributions of sky luminance and radiance of North Bangkok under standard distributions, Renew. Energy 32 (8) (2007) 1328–1345.

[6] M.T. Markou, A. Bartzokas, H.D. Kambezidis, A new statistical methodology for classification of sky luminance distributions based on scan data, Atmos. Res. 86 (3–4) (2007) 261–277.

[7] S. Wittkopf, L. Soon, Analysing sky luminance scans and predicting frequent sky patterns in Singapore, Light. Res. Technol. 39 (1) (2007) 31–51.

[8] H. Xiao, Q. Kang, J. Zhao, Y.-s. Xiao, A dynamic sky recognition method for use in energy efficient lighting design based on CIE standard general skies, Build. Environ. 45 (5) (2010) 1319–1328.

[9] M. Inanici, B. Abboushi, S. Safranek, Evaluation of sky spectra and sky models in daylighting simulations, Light. Res. Technol. (2022) 14771535221103400.

[10] C. Chatzipoulka, R. Compagnon, J. Kaempf, M. Nikolopoulou, Sky view factor as predictor of solar availability on building façades, Sol. Energy 170 (2018) 1026–1038.

[11] C. Gueymard, S. Ivanova, Progress in sky radiance and luminance modeling using circumsolar radiation and sky view factors, in: Proceedings of 12th International Conference on Solar Energy for Buildings and Industry, EuroSun–2018, Rapperswil, Switzerland, 2018.

[12] Y.K. Yi, H. Kim, Universal Visible Sky Factor: A method for calculating the three-dimensional visible sky ratio, Build. Environ. 123 (2017) 390–403.

[13] S. Lou, D.H. Li, J.C. Lam, E.W. Lee, Estimation of obstructed vertical solar irradiation under the 15 CIE Standard Skies, Build. Environ. 103 (2016) 123–133.

[14] Y. Cascone, V. Corrado, V. Serra, Calculation procedure of the shading factor under complex boundary conditions, Sol. Energy 85 (10) (2011) 2524–2539.

[15] S.M. Ivanova, Estimation of background diffuse irradiance on orthogonal surfaces under partially obstructed anisotropic sky. Part I–Vertical surfaces, Sol. Energy 95 (2013) 376–391.

[16] S.M. Ivanova, Estimation of background diffuse irradiance on orthogonal surfaces under partially obstructed anisotropic sky. Part II–Horizontal surfaces, Sol. Energy 100 (2014) 234–250.

[17] J. Li, B.E. Carlson, Y.L. Yung, D. Lv, J. Hansen, J.E. Penner, H. Liao, V. Ramaswamy, R.A. Kahn, P. Zhang, et al., Scattering and absorbing aerosols in the climate system, Nat. Rev. Earth Environ. 3 (6) (2022) 363–379.

[18] F. Plag, I. Kröger, S. Riechelmann, S. Winter, Multidimensional model to correct PV device performance measurements taken under diffuse irradiation to reference conditions, Sol. Energy 174 (2018) 431–444.

[19] N. Lindsay, Q. Libois, J. Badosa, A. Migan-Dubois, V. Bourdin, Errors in PV power modelling due to the lack of spectral and angular details of solar irradiance inputs, Sol. Energy 197 (2020) 266–278.

[20] H. Tawa, H. Saiki, Y. Ota, K. Araki, T. Takamoto, K. Nishioka, Accurate output forecasting method for various photovoltaic modules considering incident angle and spectral change owing to atmospheric parameters and cloud conditions, Appl. Sci. 10 (2) (2020) 703.

[21] M.K. Sharma, J. Bhattacharya, Dependence of spectral factor on angle of incidence for monocrystalline silicon based photovoltaic solar panel, Renew. Energy 184 (2022) 820–829.

[22] W. Gao, R.H. Grant, G.M. Heisler, J.R. Slusser, A geometric ultraviolet-B radiation transfer model applied to vegetation canopies, Agron. J. 94 (3) (2002) 475–482.

[23] R.H. Grant, G.M. Heisler, W. Gao, Photosynthetically-active radiation: sky radiance distributions under clear and overcast conditions, Agricult. Forest Meteorol. 82 (1–4) (1996) 267–292.

[24] R. Grant, G. Heisler, W. Gao, Clear sky radiance distributions in ultraviolet wavelength bands, Theor. Appl. Climatol. 56 (3) (1997) 123–135.

[25] Q. Wang, J. Tenhunen, M. Schmidt, D. Otieno, O. Kolcun, M. Droesler, Diffuse PAR irradiance under clear skies in complex alpine terrain, Agricult. Forest Meteorol. 128 (1–2) (2005) 1–15.

[26] G. Seckmeyer, M. Schrempf, A. Wieczorek, S. Riechelmann, K. Graw, S. Seckmeyer, M. Zankl, A novel method to calculate solar UV exposure relevant to vitamin D production in humans, Photochem. Photobiol. 89 (4) (2013) 974–983.

[27] E. Bruneton, A qualitative and quantitative evaluation of 8 clear sky models, IEEE Trans. Vis. Comput. Graphics 23 (12) (2016) 2641–2655.

[28] P.J. Kennelly, A.J. Stewart, General sky models for illuminating terrains, Int. J. Geogr. Inf. Sci. 28 (2) (2014) 383–406.

[29] J. Del Rocco, P.D. Bourke, C.B. Patterson, J.T. Kider, Real-time spectral radiance estimation of hemispherical clear skies with machine learned regression models, Sol. Energy 204 (2020) 48–63.

[30] A. Wilkie, P. Vevoda, T. Bashford-Rogers, L. Hošek, T. Iser, M. Kolářová, T. Rittig, J. Křivánek, A fitted radiance and attenuation model for realistic atmospheres, ACM Trans. Graph. 40 (4) (2021) 1–14.

[31] K. Tohsing, M. Schrempf, S. Riechelmann, H. Schilke, G. Seckmeyer, Measuring high-resolution sky luminance distributions with a ccd camera, Appl. Opt. 52 (8) (2013) 1564–1573.

[32] S.-I. Yun, K.-S. Kim, Sky luminance measurements using CCD camera and comparisons with Calculation models for predicting indoor illuminance, Sustainability 10 (5) (2018) 1556.

[33] P. Tregenza, R. Perez, J. Michalsky, R. Seals, B. Molineaux, P. Ineichen, Guide to recommended practice of daylight measurement, Environ. Sci. (1994).

[34] Y. Mao, C.H. Betters, B. Evans, C.P. Artlett, S.G. Leon-Saval, S. Garske, I.H. Cairns, T. Cocks, R. Winter, T. Dell, OpenHSI: A complete open-source hyperspectral imaging solution for everyone, Remote Sens. 14 (9) (2022) 2244.

[35] K.M. Gorski, E. Hivon, A.J. Banday, B.D. Wandelt, F.K. Hansen, M. Reinecke, M. Bartelmann, HEALPix: A framework for high-resolution discretization and fast analysis of data distributed on the sphere, Astrophys. J. 622 (2) (2005) 759.

[36] A. Zonca, L.P. Singer, D. Lenz, M. Reinecke, C. Rosset, E. Hivon, K.M. Gorski, healpy: equal area pixelization and spherical harmonics transforms for data on the sphere in Python, J. Open Source Softw. 4 (35) (2019) 1298.
[37] I. García, M. de Blas, J.L. Torres, The sky characterization according to the CIE Standard General sky: comparative analysis of three classification methods, Sol. Energy 196 (2020) 468–483.
[38] A.J. Marsh, PD: CIE Sky Model, 2018, https://drajmarsh.bitbucket.io/cie-sky.html. (Online; accessed 19-March-2023).
[39] D.B. Crawley, L.K. Lawrie, F.C. Winkelmann, W.F. Buhl, Y.J. Huang, C.O. Pedersen, R.K. Strand, R.J. Liesen, D.E. Fisher, M.J. Witte, et al., EnergyPlus: creating a new-generation building energy simulation program, 2001, https://energyplus.net/weather-location/north_and_central_america_wmo_region_4/USA/MN/USA_MN_Rochester.Intl.AP.726440_TMY3. (Online; accessed 19-March-2023).
[40] R. Kittler, S. Darula, Scattered sunlight determining sky luminance patterns, Renew. Sustain. Energy Rev. 62 (2016) 575–584.